Heliyon 5 (2019) e01662

Contents lists available at ScienceDirect

Heliyon

www.elsevier.com/locate/heliyon

A mathematical model for entropy generation in a Powell-Eyring nanofluid flow in a porous channel

Hammed Abiodun Ogunseye *, Precious Sibanda

University of KwaZulu-Natal, School of Mathematics, Statistics and Computer Science, Private Bag X01, Scottsville, Pietermaritzburg 3209, South Africa

ARTICLE INFO

Keywords:
Applied mathematics
Computational mathematics
Thermodynamics

ABSTRACT

The continuous generation of entropy leads to exergy destruction which reduces the performance of a physical system. Hence, entropy minimization becomes necessary. New applications of nanofluids due to their enhanced thermo-physical properties has spurred new studies into the heat transfer and entropy generation rate in nanofluids in the last decade. In this study, we investigate the heat transfer performance and entropy generation rate in a mixed convective flow of a hydromagnetic Aluminum oxide-water Powell-Eyring nanofluid flow through a vertical channel. The nanofluid dynamic viscosity adopted is based on experimental data. The combined effects of the magnetic field, nonlinear thermal radiation, viscous dissipation, suction/injection and convective cooling on the heat transfer and entropy generation were considered. The dimensionless equations describing the flow and energy balance were solved using an efficient iterative spectral local linearization method. The computational analysis of the rate of entropy generation in the channel for various flow parameters is presented. The result shows that increasing the nanoparticle volume fraction and thermal radiation parameter enhanced the temperature profiles, entropy generation and the Bejan number. The results from this study may help engineers in the optimization of thermal systems.

1. Introduction

Nanofluids are stable and uniform colloids of nanometer-sized metals or metallic oxides called nanoparticles. These fluids have a higher thermal conductivity relative to the base fluid. Choi [1] reported that the thermal conductivity of the base fluid is significantly enhanced by adding a low volume fraction of nanoparticles. Nanofluids now find applications in the enhancement of chemical engineering operations, polymer processing and petrochemical applications. A comprehensive review of other applications of nanofluids is reported in the study by Wong and De Leon [2]. In recent years, considerable attention has been focused on the study of the transport phenomenon in nanofluid flow due to their wide applications. The study of the magnetohydrodynamics (MHD) nanofluid flow past a channel was investigated by Sheikholeslami et al. [3]. They obtained a series solution to the flow equations by using the Least Square and Galerkin methods. Raza et al. [4] extended the Sheikholeslami et al. [3] model to include heat transfer analysis. The heat equation was solved using the Runge-Kutta-Fehlberg shooting technique. Hayat et al. [5] studied the MHD nanofluid flow in a rotating porous disk. Malvandi and Ganji [6] examined the thermal transport in a nanofluid within a circular microchannel. Das et al. [7] presented the radiative hydromagnetic buoyancy-induced flow and heat transfer in a nanofluid.

In these studies, emphasis was dominantly placed on the Newtonian constitutive model. However, in recent years, the focus of researchers has been centered on the study of non-Newtonian fluids due to their industrial, technological and medical applications. These fluids exhibit complex relations between stress and the rate of strain, hence, they deviate from the Newton's law of viscosity. A single constitutive relation cannot be used to understand the complex nature of non-Newtonian fluids. On account of this fact, several non-Newtonian constitutive models have been put forward by scientist, among which but not limited to, are the power-law fluid model, Casson fluid model, viscoelastic fluid model and Powell-Eyring fluid model. Researchers have focused attention on the Powell-Eyring model [8] due to its advantages over other non-Newtonian models. The Powell-Eyring model is derived from the kinetics theory of fluids and not on an empirical relation. Further, under certain shear rates, the model reduces to a Newtonian model. The flow and heat transport in a Powell-Eyring fluid has been studied by many researchers. Tanveer et al. [9] studied the mixed convection peristaltic flow of a Powell-Eyring nanofluid in a curved channel. Khan and Pop [10] investigated the heat and mass transfer in a nanofluid past a

* Corresponding author.
E-mail address: ogunseyehammed@gmail.com (H.A. Ogunseye).

https://doi.org/10.1016/j.heliyon.2019.e01662
Received 6 January 2019; Received in revised form 3 April 2019; Accepted 2 May 2019

stretching plate. Agbaje et al. [11] studied the transient developing flow of a Powell-Eyring nanofluid over a shrinking plane. The effects of slip conditions on the flow of a Powell-Eyring nanofluid was discussed by Hina [12]. Hayat et al. [13] reported the heat transport in a radiative Powell-Eyring nanofluid.

Exergy loss is a major challenge in many industrial processes. Recently, the interest of many researchers has shifted towards entropy generation analysis in a nanofluid flow. This is important in many thermal engineering processes, because the continuous generation of entropy eventually leads to exergy destruction in the system. Therefore, the optimization of the performance of industrial and engineering processes is necessary and could be achieved by minimizing entropy generation [14]. The second law of thermodynamics is an efficient and accurate tool for optimizing a given system as opposed to the first law of thermodynamics. Following Bejan [14] several studies on the entropy generation minimization based on second law thermodynamics analysis have appeared in the literature. Pakdemirli and Yilbas [15] analyzed the entropy generation in a third-grade fluid. Das et al. [16] studied the entropy generation in the hydrodynamics pseudo-plastic in a nanofluid flow through a porous channel. Ting et al. [17] discussed the effect of viscous dissipation on the entropy generation in a nanofluid flow in a channel. The exact solution to the study of entropy generation in the magnetohydrodynamic fluid flow was presented by Ibáñez [18]. López et al. [19] reported on the entropy generation in a magnetohydrodynamic flow of a nanofluid in a porous channel. They considered the effect of non-linear thermal radiation and convective-radiative boundary conditions. Makinde and Eegunjobi [20] studied numerically, the impact of convective heating on the entropy generation rate of a steady flow between two permeable walls. Recently, Nagaraju et al. [21] considered the effect of suction and magnetic field effects on the entropy generation in the fluid flow through a circular pipe. The homotopy perturbation method was used for the solution of the flow equations. Computational simulation on the role of magnetic forces on ferrofluid second law treatment was scrutinized by Sheikholeslami [22]. Jangili et al. [23] studied the entropy generation in a couple stress fluid flow. The homotopy analysis method was utilized for their analysis. Further studies on the minimization of entropy generation in the fluid flow using second law analysis under different geometry are reported in [24, 25, 26, 27, 28].

The aim of this study is to examine the entropy generation in the flow of a Powell-Eyring nanofluid in a porous channel. The mathematical formulation includes the effects of hydrodynamic slip, viscous dissipation, nonlinear thermal radiation and convective boundary conditions. The flow equations are solved numerically using an iterative spectral local linearization method. The findings may be useful in optimizing thermal engineering processes such as crude pyrolysis.

2. Model

2.1. Mathematical formulation and analysis

The mixed convective laminar, viscous flow of an incompressible Powell-Eyring nanofluid through a vertical channel separated by a distance h apart is considered. The schematic diagram for the flow geometry is shown in Fig. 1. It is assumed that an external transverse and uniform magnetic field of strength B_0 is applied parallel to the flow field. We assumed the magnetic Reynold number and induced electric field to be negligible.

With the above assumptions, the momentum and heat balance equations for the Powell-Eyring nanofluid flow are written as [11, 19]

$$\rho_{nf}V_0\frac{d\bar{u}}{d\bar{y}} = -\frac{d\bar{P}}{d\bar{x}} + \left(\mu_{nf}+\frac{1}{bc}\right)\frac{d^2\bar{u}}{d\bar{y}^2} - \frac{1}{2bc^3}\left(\frac{d\bar{u}}{d\bar{y}}\right)^2\frac{d^2\bar{u}}{d\bar{y}^2} - \sigma_{nf}B_0^2\bar{u} + g(\rho\beta)_{nb}\left(T-T_0\right), \tag{1}$$

$$(\rho C_p)_{np}V_0\frac{d\bar{T}}{d\bar{y}} = k_{nf}\frac{d^2\bar{T}}{d\bar{y}^2} + \frac{16\sigma_s}{3k_m}\frac{d}{d\bar{y}}\left(\bar{T}^3\frac{d\bar{T}}{d\bar{y}}\right) + \left(\mu_{nf}+\frac{1}{bc}\right)\left(\frac{d\bar{u}}{d\bar{y}}\right)^2 - \frac{1}{6bc^3}\left(\frac{d\bar{u}}{d\bar{y}}\right)^4 + \sigma_{nf}B_0^2\bar{u}^2, \tag{2}$$

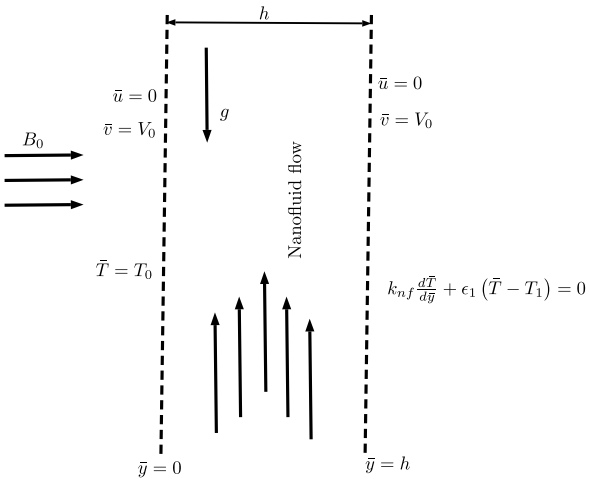

Fig. 1. Geometry of the flow.

where V_0 is the uniform suction/injection velocity at the channel plates, $\bar{u}$ is the axial velocity, μ_{nf} is the dynamic viscosity of nanofluid, b and c are fluid constants, σ_{nf} is the nanofluid electrical conductivity, g is the gravitational acceleration, ρ_{nf} is the nanofluid density, β_{nb} is the thermal expansion coefficient of nanofluid, $\bar{T}$ is the nanofluid temperature, T_0 is the ambient temperature, $(C_p)_{nb}$ is the heat capacitance of nanofluid, k_{nf} is nanofluid thermal conductivity, σ_s is the Stefan-Boltzman constant and k_m is the mean absorption coefficient.

The relevant boundary conditions for Eqs. (1) and (2) are:

$$\bar{u}=0, \quad \bar{T}=T_0, \quad \text{at} \quad \bar{y}=0, \tag{3}$$

$$\bar{u}=0, \quad k_{nf}\frac{d\bar{T}}{d\bar{y}}+\epsilon_1\left(\bar{T}-T_1\right)=0, \quad \text{at} \quad \bar{y}=h \tag{4}$$

where ϵ_1 is the convective heat transfer coefficients.

Nguyen et al. [29] proposed a new model for the dynamic viscosity of Al_2O_3-water nanofluid based on their experimental data. Adopting the Nguyen et al. [29] model, the nanofluid viscosity can be represented by the relation

$$\frac{\mu_{nf}}{\mu_{bf}} = 1+0.025\phi+0.015\phi^2. \tag{5}$$

The density, thermal expansion coefficient, electrical conductivity, specific heat capacity and thermal conductivity of the nanofluid are determined by the expressions (see Khanafer and Vafai [30] and Das and Jana [31]),

$$\left.\begin{aligned}
\frac{\rho_{nf}}{\rho_{bf}} &= 1-\phi+\phi\frac{\rho_s}{\rho_{bf}},\\
\frac{(\rho\beta)_{nf}}{(\rho\beta)_{bf}} &= 1-\phi+\phi\frac{(\rho\beta)_s}{(\rho\beta)_{bf}},\\
\frac{\sigma_{nf}}{\sigma_{bf}} &= \left[1+\frac{3\left(\frac{\sigma_s}{\sigma_{bf}}-1\right)\phi}{\left(\frac{\sigma_s}{\sigma_{bf}}+2\right)-\left(\frac{\sigma_s}{\sigma_{bf}}-1\right)\phi}\right],\\
\frac{(\rho C_p)_{nf}}{(\rho C_p)_{bf}} &= 1-\phi+\phi\frac{(\rho C_p)_s}{(\rho C_p)_{bf}},\\
\frac{k_{nf}}{\kappa_{bf}} &= \frac{k_s+2k_{bf}-2\left(k_{bf}-k_s\right)\phi}{k_s+2k_{bf}+\left(k_{bf}-k_s\right)\phi}.
\end{aligned}\right\} \tag{6}$$

In Eqs. (5) and (6), ϕ denotes the nanoparticle volume fraction, the subscripts bf and s represent the properties of the base fluid and nanoparticles respectively. The thermo-physical properties of the Al_2O_3-water nanofluid are presented in Table 1.

Table 1
Thermo-physical properties of water and Al_2O_3 [16].

	ρ	C_p ($Jkg^{-1}K^{-1}$)	k ($Wm^{-1}K^{-1}$)	$\beta\times10^5$ (K^{-1})	σ (Sm^{-1})
Water	997.1	4179	0.613	21	5.5×10^{-6}
Al_2O_3	3970	765	40	0.85	35×10^6

In order to express Eqs. (1), (2), (3) and (4) in a nondimensional form, it is necessary to define the dimensionless variables accordingly, and the following variables are chosen [19, 23, 26]:

$$y=\frac{\bar{y}}{h},\quad x=\frac{\bar{x}}{h},\quad u=\frac{\bar{u}h\rho_{bf}}{\mu_{bf}},P=\frac{\bar{P}h^2\rho_{bf}}{\mu_{bf}^2},\quad \theta=\frac{\bar{T}-T_0}{T_1-T_0}. \tag{7}$$

Using Eq. (7), Eqs. (1), (2), (3) and (4) yields the following dimensionless form;

$$\left(1+0.025\phi+0.015\phi^2+\lambda\right)\frac{d^2u}{dy^2}-\delta\lambda\left(\frac{du}{dy}\right)^2\frac{d^2u}{dy^2}-\frac{\sigma_{nf}}{\sigma_{bf}}Ha^2u + \frac{(\rho\beta)_{nf}}{(\rho\beta)_{bf}}Gr\theta-\frac{\rho_{nf}}{\rho_{bf}}Re\frac{du}{dy}+G=0, \tag{8}$$

$$\left(\frac{k_{nf}}{k_{bf}}+Nr\left[\left(\theta_w-1\right)\theta+1\right]^3\right)\frac{d^2\theta}{dy^2} + 3Nr\left(\theta_w-1\right)\left[\left(\theta_w-1\right)\theta+1\right]^2\left(\frac{d\theta}{dy}\right)^2-\frac{\left(C_p\right)_{nf}}{\left(C_p\right)_{bf}}RePr\frac{d\theta}{dy} + Br\left[\left(1+0.025\phi+0.015\phi^2+\lambda\right)\left(\frac{du}{dy}\right)^2-\frac{\delta\lambda}{3}\left(\frac{du}{dy}\right)^4+\frac{\sigma_{nf}}{\sigma_{bf}}Ha^2u^2\right] =0, \tag{9}$$

$$u=0,\quad \theta=0,\quad \text{at}\quad y=0, \tag{10}$$

$$u=0,\quad \frac{k_{nf}}{k_{bf}}\frac{d\theta}{dy}+\gamma(\theta-1)=0,\quad \text{at}\quad y=1, \tag{11}$$

where λ and δ are fluid constants, Ha is the Hartmann number, Gr is the Grashof number, Re is the suction/injection parameter, G is the axial pressure gradient parameter, Nr is the thermal radiation parameter, θ_w is the temperature ratio parameter, Pr is the Prandtl number, Br is the Brinkman number which is related to the Eckert number, γ is the Biot number. These parameters are defined as;

$$\lambda=\frac{1}{bc\mu_{bf}},\quad \delta=\frac{\mu_{bf}^2}{2c^2\rho_{bf}^2h^4},\quad Ha^2=\frac{\sigma_{bf}B_0h^2}{\mu_{bf}},$$
$$Gr=\frac{g\beta_{bf}\rho_{bf}^2\left(T_1-T_0\right)h^3}{\mu_{bf}^2},\quad Re=\frac{\rho_{bf}V_0h}{\mu_{bf}},\quad \gamma=\frac{h\epsilon_1}{k_{bf}},$$
$$G=-\frac{dP}{dx},\quad Nr=\frac{16\sigma_sT_0^3}{3k_mk_{bf}},\quad \theta_w=\frac{T_1}{T_0},\quad Pr=\frac{\mu_{bf}\left(C_p\right)_{bf}}{k_{bf}},$$
$$Br=\frac{\mu_{bf}^3}{\rho_{bf}k_{bf}\left(T_1-T_0\right)h^2},\qquad \gamma_2=\frac{h\epsilon_2}{k_{bf}}. \tag{12}$$

Other important physical properties are the skin-friction coefficient C_f and local Nusselt number Nu which are defined as follows:

$$C_f=\frac{\rho_{bf}h^2\tau_w}{\mu_{bf}};\quad \tau_w=\left(\mu_{nf}+\frac{1}{bc}\right)\left(\frac{d\bar{u}}{d\bar{y}}\right)-\frac{1}{6bc^3}\left(\frac{d\bar{u}}{d\bar{y}}\right)^3\Big|_{\bar{y}=0}=0, \tag{13}$$

$$Nu=\frac{hq_w}{k_{bf}\left(T_1-T_0\right)};\quad q_w=-\left(k_{nf}+\frac{16\sigma_s}{3k_m}\bar{T}^3\right)\frac{d\bar{T}}{d\bar{y}}\Big|_{\bar{y}=0}. \tag{14}$$

In terms of Eq. (7), the dimensionless forms of Eqs. (13) and (14) are given by

$$C_f=\left(1+0.025\phi+0.015\phi^2+\lambda\right)\frac{du}{dy}\Big|_{y=0}-\frac{\delta\lambda}{3}\left(\frac{du}{dy}\Big|_{y=0}\right)^3, \tag{15}$$

$$Nu=-\left(\frac{k_{nf}}{k_{bf}}+Nr\right)\frac{d\theta}{dy}\Big|_{y=0}. \tag{16}$$

2.2. Entropy generation

In many thermodynamic processes, energy management is of great concern when a large amount of energy is dissipated as heat. Hence, it is important to investigate the entropy generation of the system. Conforming with Bejan [14], the entropy generation rate per volume in the nanofluid flow in the channel can be expressed as

$$S_G=\underbrace{\frac{1}{T_0^2}\left(k_{nf}+\frac{16\sigma_s\bar{T}^3}{3k_m}\right)\left(\frac{d\bar{T}}{d\bar{y}}\right)^2}_{\text{First term}} + \underbrace{\frac{1}{T_0}\left[\left(\mu_{nf}+\frac{1}{bc}\right)\left(\frac{d\bar{u}}{d\bar{y}}\right)^2-\frac{1}{6bc^3}\left(\frac{d\bar{u}}{d\bar{y}}\right)^4\right]}_{\text{Second term}}+\underbrace{\frac{\sigma_{nf}B_0^2}{T_0}\bar{u}^2}_{\text{Third term}}. \tag{17}$$

In Eq. (17) the first term represents the heat entropy generation due to heat transfer and thermal radiation, the second term denotes the entropy production due to fluid frictional interaction and finally, the third term indicates the entropy generation due to magnetic flied.

Using Eq. (7), we can rewrite Eq. (17) as

$$Ns=\frac{T_0h^2S_G}{k_{bf}\left(T-1-T_0\right)^2}=\left(\frac{k_{nf}}{k_{bf}}+Nr\left[\left(\theta_w-1\right)\theta+1\right]^3\right)\left(\frac{d\theta}{dy}\right)^2 + \frac{Br}{\theta_w-1}\left[\left(1+0.025\phi+0.015\phi^2+\lambda\right)\left(\frac{du}{dy}\right)^2 - \frac{\delta\lambda}{3}\left(\frac{du}{dy}\right)^4+\frac{\sigma_{nf}}{\sigma_{bf}}Ha^2u^2\right] \tag{18}$$

Let us define the following variables

$$N_f=\frac{Br}{\theta_w-1}\left[\left(1+0.025\phi+0.015\phi^2+\lambda\right)\left(\frac{du}{dy}\right)^2-\frac{\delta\lambda}{3}\left(\frac{du}{dy}\right)^4 + \frac{\sigma_{nf}}{\sigma_{bf}}Ha^2u^2\right],$$
$$N_h=\left(\frac{k_{nf}}{k_{bf}}+Nr\left[\left(\theta_w-1\right)\theta+1\right]^3\right)\left(\frac{d\theta}{dy}\right)^2, \tag{19}$$

then N_f is the irreversibility due to combined effects of viscous dissipation and magnetic field and N_h is the heat transfer with thermal radiation irreversibility.

The Bejan number can be used to determine the relative effects of the heat transfer irreversibility and irreversibility due to combined effects of viscous dissipation and magnetic field in the entropy generation. Thus, we define the Bejan, number, Be, as (see Bejan [14])

$$Be=\frac{N_h}{N_h+N_f}=\frac{1}{1+M}, \tag{20}$$

where $M=N_f/N_h$ is the irreversibility ratio.

3. Calculation

3.1. Numerical solution

In this section, an efficient iterative spectral local linearization method (SLLM) proposed by Motsa [32] is used to numerically integrate the coupled non-linear differential Eqs. (8) and (9) with the boundary conditions Eqs. (10) and (11). To apply this technique, we consider the following non-linear differential operators

$$\Omega_u=\left(1+0.025\phi+0.015\phi^2+\lambda\right)u_n''-\delta\lambda\left(u'-n\right)^2u_n''-\frac{\sigma_{nf}}{\sigma_{bf}}Ha^2u_n + \frac{(\rho\beta)_{nf}}{(\rho\beta)_{bf}}Gr\theta_n-\frac{\rho_{nf}}{\rho_{bf}}Reu_n'+G \tag{21}$$

$$\Omega_\theta = \left(\frac{k_{nf}}{k_{bf}} + Nr\left[\left(\theta_w - 1\right)\theta_n + 1\right]^3\right)\theta_n'' + 3Nr\left(\theta_w - 1\right)\left[\left(\theta_w - 1\right)\theta_n + 1\right]^2\left(\theta_n'\right)^2 - \frac{\left(C_p\right)_{nf}}{\left(C_p\right)_{bf}}RePr\theta_n' + Br\left[\left(1 + 0.025\phi + 0.015\phi^2 + \lambda\right)\left(u_n'\right)^2 - \frac{\delta\lambda}{3}\left(u_n'\right)^4 + \frac{\sigma_{nf}}{\sigma_{bf}}Ha^2u_n^2\right] \tag{22}$$

where the prime denotes derivative with respect to y.

Eqs. (21) and (22) can be decoupled according to the following algorithm;

1. From Ω_u, find u_{n+1} assuming that θ_n is known from the previous iteration.
2. Solve for θ_{n+1} from Ω_θ using the updated solution of f_n.
3. Subsequent iterative solutions are obtained by repeating step 1 and 2.

In the framework of the SLLM, the following iterative scheme is obtained

$$a_{1,n}u_{n+1}'' + a_{2,n}u_{n+1}' + a_{3,n}u_{n+1} = R^u, \tag{23}$$

$$a_{4,n}\theta_{n+1}'' + a_{5,n}\theta_{n+1}' + a_{6,n}\theta_{n+1} = R^\theta, \tag{24}$$

$$u_{n+1}(0) = 0, \quad \theta_{n+1}(0) = 0, \tag{25}$$

$$u_{n+1}(1) = 0, \quad \frac{k_{nf}}{k_{bf}}\theta_{n+1}'(1) + \gamma\left(\theta_{n+1}(1) - 1\right) = 0. \tag{26}$$

The coefficients in Eqs. (23) and (24) along with their right hand sides are defined as follows

$$a_{1,n} = \frac{\partial\Omega_u}{\partial u_n''} = 1 + 0.025\phi + 0.015\phi^2 + \lambda - \delta\lambda u_n'^2,$$

$$a_{2,n} = \frac{\partial\Omega_u}{\partial u_n'} = -2\lambda\delta u_n'u_n'' - \frac{\rho_{nf}}{\rho_{bf}}Re$$

$$a_{3,n} = \frac{\partial\Omega_u}{\partial u_n} = -\frac{\sigma_{nf}}{\sigma_{bf}}Ha^2, \quad a_{4,n} = \frac{\partial\Omega_\theta}{\partial\theta_n''} = \left(\frac{k_{nf}}{k_{bf}} + Nr\left[\left(\theta_w - 1\right)\theta_n + 1\right]^3\right)$$

$$a_{5,n} = \frac{\partial\Omega_\theta}{\partial\theta_n'} = 6Nr\left(\theta w - 1\right)\left(1 + \left(\theta w - 1\right)\theta_n\right)^2\theta_n\theta_n' - \frac{\left(C_p\right)_{nf}}{\left(C_p\right)_{bf}}RePr \tag{27}$$

$$a_{6,n} = \frac{\partial\Omega_\theta}{\partial\theta_n} = 3Nr\left(\theta_w - 1\right)\left[\left(\theta_w - 1\right)\theta_n + 1\right]^2\theta_n'' + 6Nr\left(\theta_w - 1\right)^2\left[\left(\theta_w - 1\right)\theta_n + 1\right]\left(\theta_n'\right)^2$$

$$R^u = a_{1,n}u_n'' + a_{2,n}u_n' + a_{3,n}u_n - \Omega_f, \quad R^\theta = a_{4,n}\theta_n'' + a_{5,n}\theta_n' + a_{6,n}\theta_n - \Omega_\theta.$$

The Eqs. (23), (24), (25), (26) and (26), are solved numerically using the Chebyshev pseudo-spectral technique. To apply this method, we first map the interval $[0,1]$ to $[-1,1]$ using the transformation $y = (\xi + 1)/2$ for $\xi \in [-1,1]$. Then, we discretize using Chebyshev-Gauss-Labatto collocation points

$$\xi_k = \cos\left(\frac{\pi k}{N}\right), \qquad k = 0,1,\ldots,N; \quad -1 \le \xi \le 1. \tag{28}$$

The derivatives of $u(y)$ and $\theta(y)$ are computed using the Chebyshev differentiation matrix D (see [33]), at the collocation points as a matrix vector product, that is:

$$\frac{du}{dy} = \sum_{i=0}^{\bar{N}} D_{ij}f\left(\xi_i\right) = \mathbf{DF}, \qquad j = 0,1,2,\ldots,\bar{N}, \tag{29}$$

$$\frac{d\theta}{dy} = \sum_{i=0}^{\bar{N}} D_{ij}f\left(\xi_i\right) = \mathbf{D\Theta}, \qquad j = 0,1,2,\ldots,\bar{N}, \tag{30}$$

where $\bar{N}+1$ is the number of collocation points, $\mathbf{D} = 2D$, $\mathbf{F} = \left[u\left(\xi_0\right), u\left(\xi_1\right), \ldots, u\left(\xi_{\bar{N}}\right)\right]^T$ and $\mathbf{\Theta} = \left[\theta\left(\xi_0\right), \theta\left(\xi_1\right), \ldots, \theta\left(\xi_{\bar{N}}\right)\right]^T$ are vector functions at the collocation points. The second order derivatives of u and θ can be computed as the powers of $\mathbf{D}$, that is, $\theta''(y) = \mathbf{D}^2\theta(y)$ and $u''(y) = \mathbf{D}^2u(y)$.

Substituting Eqs. (28), (29) and (30) into Eqs. (23), (24), (25) and (26) and imposing the boundary conditions, gives the following decoupled matrices

$$\begin{bmatrix} 1 & \ldots & 0 \\ \mathrm{diag}[a_{1,n}]\mathbf{D}^2 + \mathrm{diag}[a_{2,n}]\mathbf{D} + \mathrm{diag}[a_{3,n}]\mathbf{I} \\ 0 & \ldots & 1 \end{bmatrix}\begin{bmatrix} u_{n+1}(\xi_0) \\ u_{n+1}(\xi_1) \\ \vdots \\ u_{n+1}(\xi_{\bar{N}-1}) \\ u_{n+1}(\xi_{\bar{N}}) \end{bmatrix} = \begin{bmatrix} 0 \\ R_{n+1}^f(\xi_1) \\ \vdots \\ R_{n+1}^f(\xi_{\bar{N}-1}) \\ 0 \end{bmatrix}, \tag{31}$$

$$\begin{bmatrix} 1 & \ldots & 0 \\ \mathrm{diag}[a_{4,n}]\mathbf{D}^2 + \mathrm{diag}[a_{5,n}]\mathbf{D} + \mathrm{diag}[a_{6,n}]\mathbf{I} \\ \frac{k_{nf}}{k_{bf}}\mathbf{D} + \gamma\mathbf{I} \end{bmatrix}\begin{bmatrix} \theta_{n+1}(\xi_0) \\ \theta_{n+1}(\xi_1) \\ \vdots \\ \theta_{n+1}(\xi_{\bar{N}-1}) \\ \theta_{n+1}(\xi_{\bar{N}}) \end{bmatrix} = \begin{bmatrix} 0 \\ R_{n+1}^\theta(\xi_1) \\ \vdots \\ R_{n+1}^\theta(\xi_{\bar{N}-1}) \\ \gamma \end{bmatrix}, \tag{32}$$

where $\mathbf{I}$ is an identity matrix of dimension $(\bar{N}+1)\times(\bar{N}+1)$ and diag[] denotes a diagonal matrix.

4. Results & discussion

The nanofluid velocity profiles, temperature profiles, entropy generation rate and Bejan number for distinct values of the fluid parameter λ, Hartmann number Ha, Grashof number Gr, suction/injection parameter Re, thermal radiation parameter Nr, temperature ratio parameter θ_w, Brinkman number Br and Biot number γ are presented in Figs. 2, 3, 4, 5, 6, 7, 8, 9 and 10 and discussed based on physical laws. In these profiles, unless otherwise stated, we have assigned the following default values to the parameters: $\lambda = Ha = Gr = G = Re = Nr = Br = \gamma = 1$, $\theta_w = 1.5$ and $Pr = 6.97$.

Fig. 2A–D represents the effects of various values of the nanoparticle fraction volume ranging from $0 \le \phi \le 0.3$ on the velocity profiles, temperature profiles, entropy generation rate and Bejan number. In general, a parabolic trajectory is obtained for the nanofluid velocity profiles with the maximum value attained near the centerline. Fig. 2A shows that as the nanoparticle volume fraction increases, there is a corresponding decrease in the nanofluid flow. This is physically correct since increasing volume fraction would have a direct impact on the internal viscous shear stresses which in-turn shortens the inter-molecular forces between the fluid particles. An increment in the volume fraction of the nanoparticle leads to a further increment in the temperature profiles close the left permeable wall in the region of $y \in [0, 0.6]$. Thereafter, the temperature profile decreases in the rest of the region towards the right permeable wall. Interestingly, we observed that entropy generation rate decreases with an increase in the nanoparticle volume fraction while the Bejan number is an increasing function of the nanoparticle volume fraction as illustrated in Fig. 2C and D respectively.

The effect of varying the fluid material parameter, λ in the range $0 \le \lambda \le 1.5$ on the nanofluid velocity profiles, temperature profiles, entropy generation rate and Bejan number is displayed in Fig. 3A to C. We observed that as the material fluid parameter increases, there is a decrease in the nanofluid dynamic viscosity, hence, the fluid flow in the channel is reduced as represented in Fig. 3A. It is worth mentioning that $\lambda = 0$ corresponds to the Newtonian case and the velocity profiles

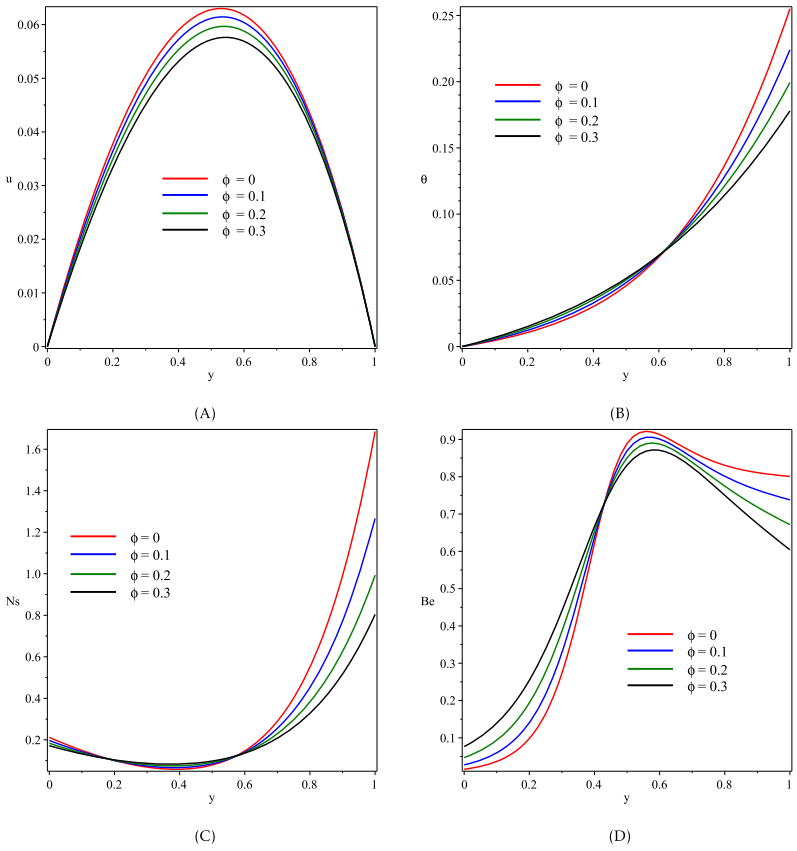

Fig. 2. Effect of varying the nanoparticle volume fraction on the nanofluid (A) velocity profiles, (B) temperature profiles, (C) entropy generation rate, (D) Bejan number.

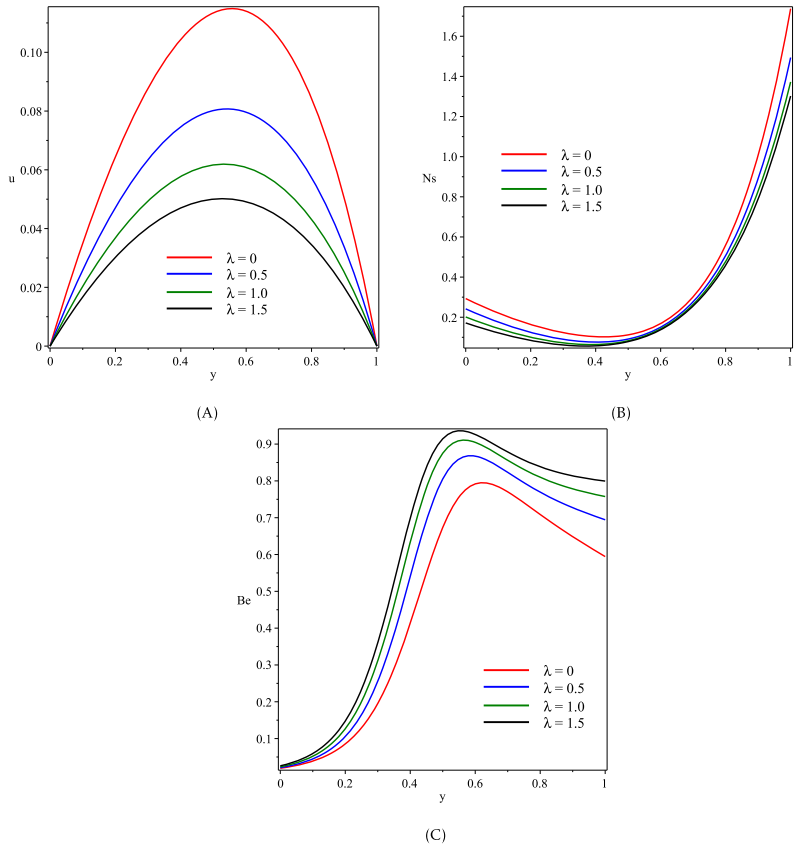

Fig. 3. Effect of varying the fluid material parameter on the nanofluid (A) velocity profiles, (B) entropy generation rate, (C) Bejan number.

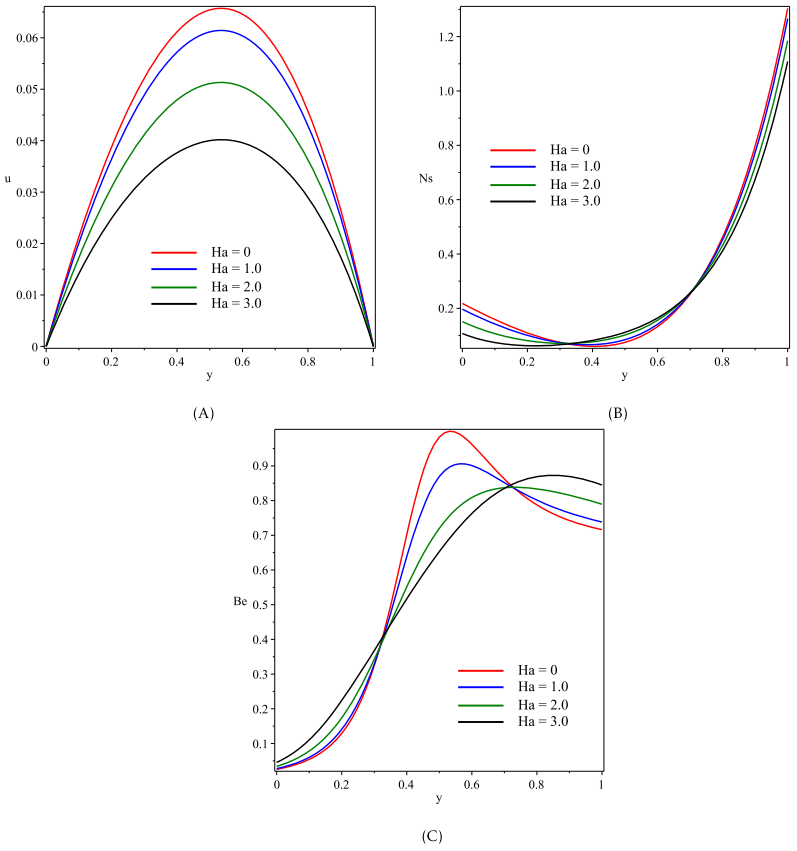

Fig. 4. Effect of increasing the Hartmann number on the nanofluid (A) velocity profiles, (B) entropy generation rate, (C) Bejan number.

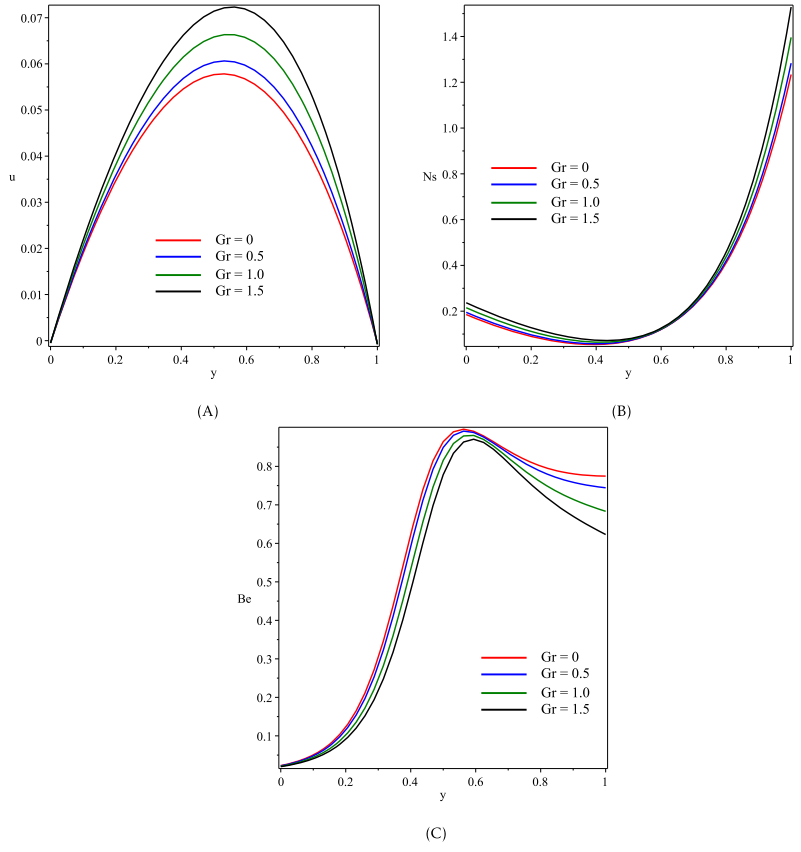

Fig. 5. Effect of increasing the Grashof number on the nanofluid (A) velocity profiles, (B) entropy generation rate, (C) Bejan number.

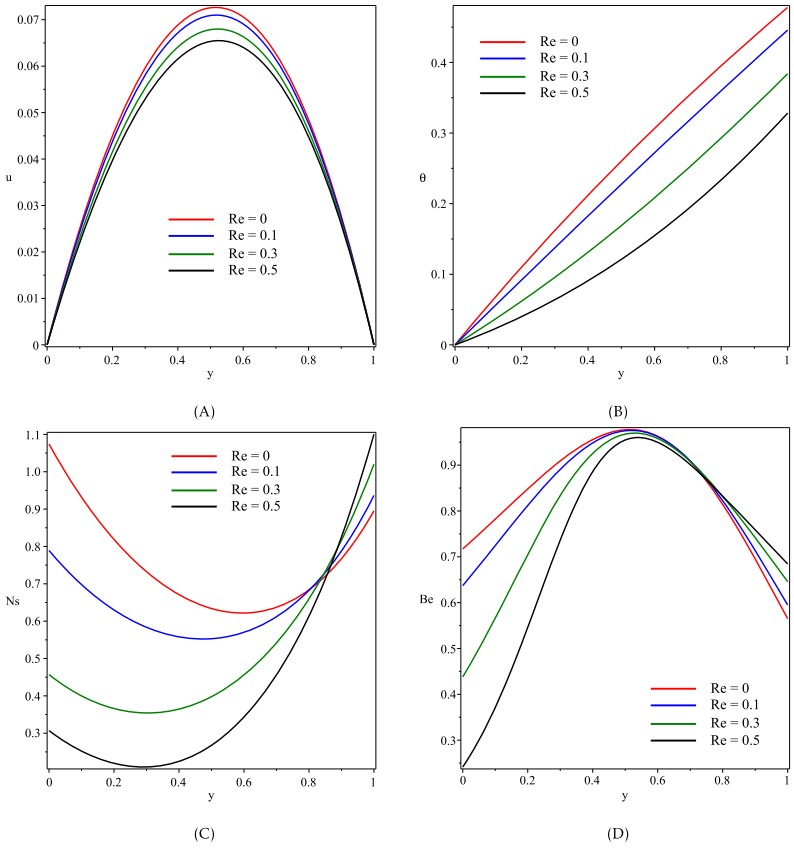

Fig. 6. Effect of varying the suction/injection Reynold number on the nanofluid (A) velocity profiles, (B) temperature profiles, (C) entropy generation rate, (D) Bejan number.

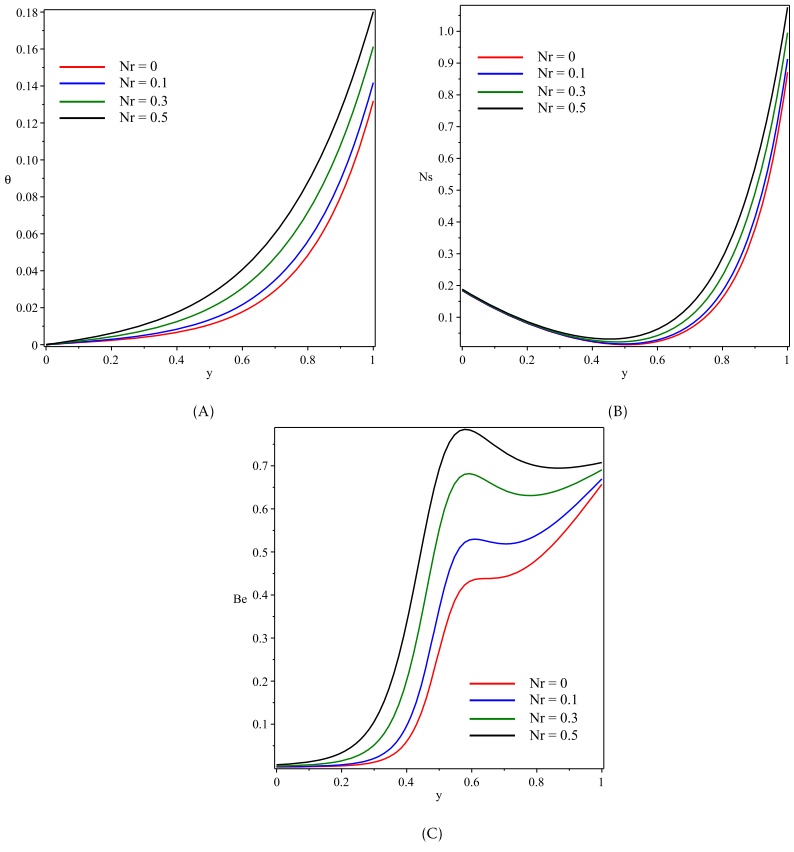

Fig. 7. Effect of varying the thermal radiation parameter on the nanofluid (A) temperature profiles, (B) entropy generation rate, (C) Bejan number.

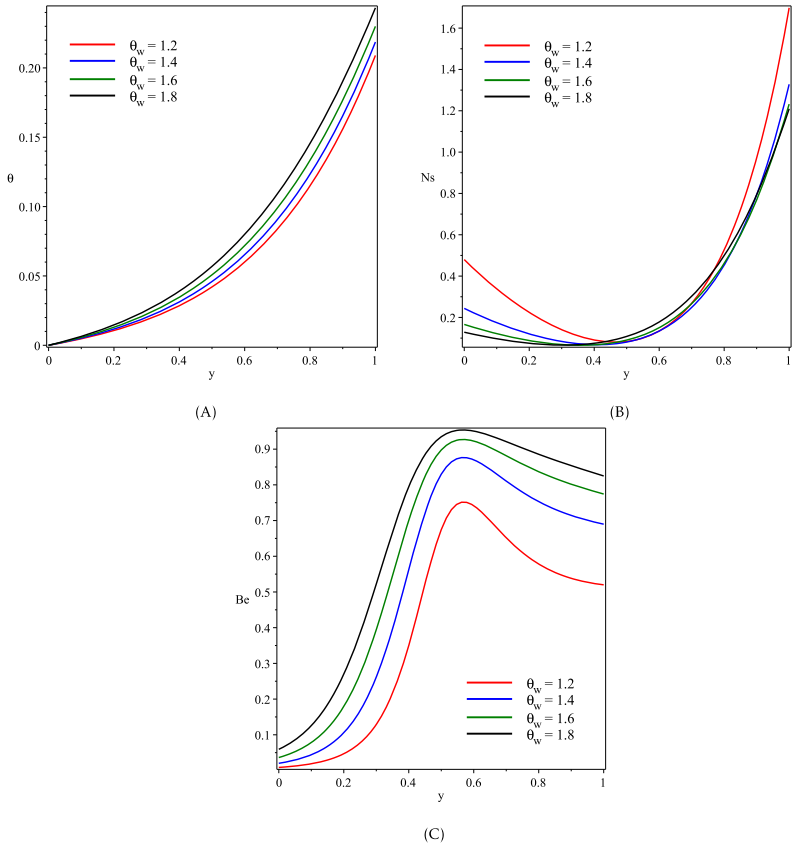

Fig. 8. Effect of varying the temperature ratio parameter on the nanofluid (A) temperature profiles, (B) entropy generation rate, (C) Bejan number.

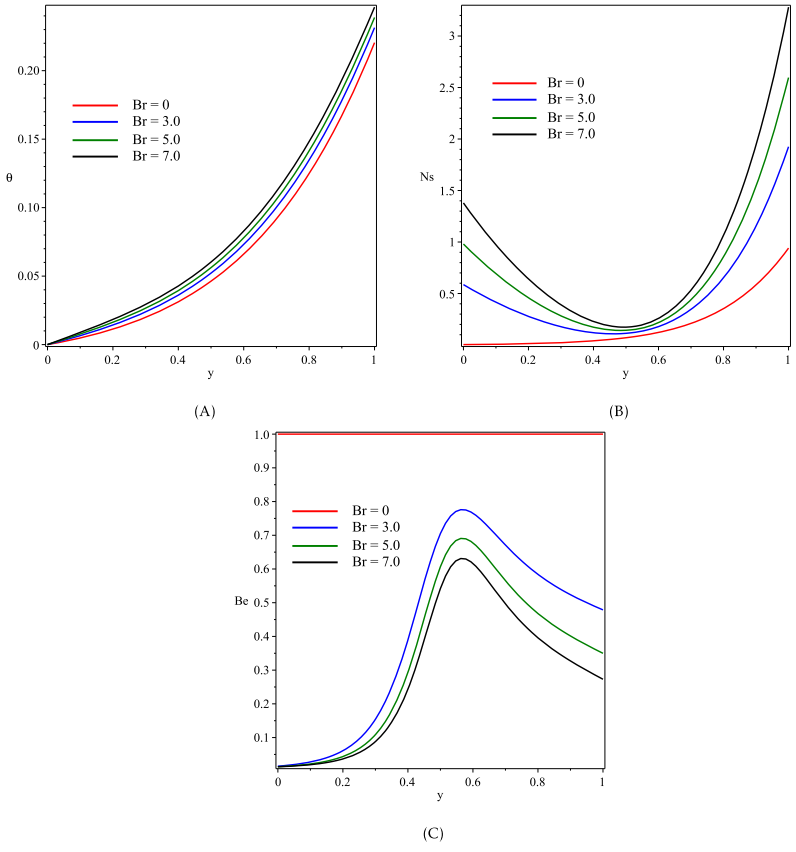

Fig. 9. Effect of varying the Brinkman number on the nanofluid (A) temperature profiles, (B) entropy generation rate, (C) Bejan number.

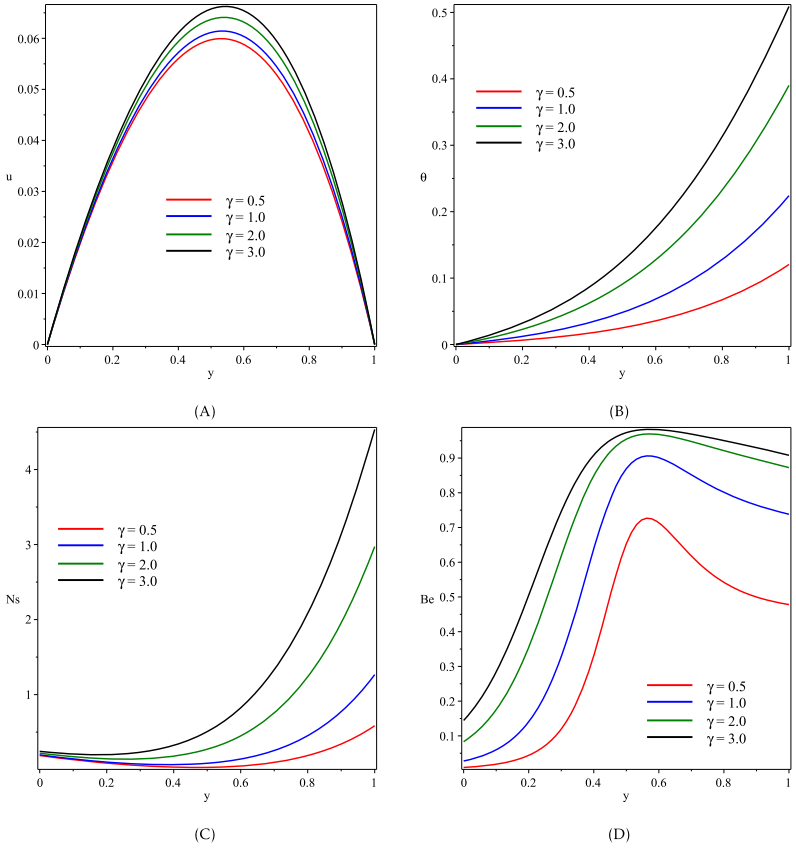

Fig. 10. Effect of varying the Biot number on the nanofluid (A) velocity profiles, (B) temperature profiles, (C) entropy generation rate, (D) Bejan number.

attained a maximum value for this case. Fig. 3B shows that the entropy generation number decreases with an increase in the fluid material parameter. This can be associated with the damping effect of the fluid material parameter on the nanofluid flow, thus, minimizing the entropy in the channel. It is easily seen from Fig. 3C that the Bejan number increases as the fluid material parameter increases.

We examined the effect of the transverse magnetic field on the nanofluid velocity, entropy generation and Bejan number. The velocity profiles, entropy generation rate and Bejan number for different values of the Hartmann number in the range $0 \leq Ha \leq 3$ are given in Fig. 4A to C. We observed that the flow in the channel decreases with an increase in the magnitude of the magnetic field intensity. Physically, this observation is correct, since, the nanofluid particles aggregate under the Lorentz dipolar forces from the transversely placed magnetic field. Interestingly, Fig. 4B shows that, the entropy generation number decreases as the Hartmann number increases close to the permeable wall, in the region $0 \leq y \leq 0.3$ and between $0.3 \leq y \leq 0.7$ the entropy generation number is an increasing function of the Hartmann number, thereafter, the entropy generation number decreases as the Hartmann number increases. The opposite trend is observed in Fig. 4C for increasing the Bejan number. Fig. 4C implies that the irreversibility due to fluid friction in the channel is higher than the heat transfer irreversibility in the region $0 \leq y \leq 0.3$ and $0.7 \leq y \leq 1$ while in the region $0.3 \leq y \leq 0.7$, the heat transfer irreversibility is higher than the irreversibility due to fluid friction.

The effect of varying the Grashof number in the range of $0 \leq Gr \leq 1.5$ on the nanofluid velocity profiles, entropy generation number and Bejan number is shown in Fig. 5A to C. We observed that the nanofluid velocity profile increases as the magnitude of the Grashof number increases as depicted in Fig. 5A. This is physically true because increasing the value of the Grashof number reduces the nanofluid dynamic viscosity. These increments lead to an increase in the volumetric thermal expansion in the channel which further enhances the nanofluid flow. Entropy generation number increases as the Grashof number increases as seen in Fig. 5B. Fig. 5C indicates that the Bejan number decreases as the value of the Grashof number increases. This result shows that the irreversibility due to frictional forces and magnetic field dominates the irreversibility due to heat transfer in the channel.

Fig. 6A to C shows the influence of the suction/injection Reynolds number on the nanofluid velocity profiles, temperature profiles, entropy generation number and the Bejan number. The value of the suction/injection Reynolds number varies in the range $0 \leq Re \leq 0.5$. We observed that as the Reynolds number increases, both the fluid injection at the left permeable wall and the fluid suction at the right permeable wall also increase, hence the velocity profile decreases as shown in Fig. 6A. It is evident from Fig. 6B that the nanofluid temperature profiles decreases with an increase in the suction/injection Reynolds number. Within the region of $0 \leq y \leq 0.85$, both the entropy generation number and the Bejan number decreases with an increase in suction/injection Reynolds number, however, there is a change in trend close to the right permeable wall in the region of $0.85 \leq y \leq 1$ as depicted in Fig. 6C to D.

The effect of different values of the thermal radiation parameter on the nanofluid temperature profiles, entropy generation number and Bejan number are displayed in Fig. 7A to C. From Fig. 7A, the nanofluid temperature profiles are enhanced with the thermal radiation parameter. The physical reason for this observed trend is that, for a higher value of the radiation parameter, more heat is transferred to the nanofluid since the mean absorption coefficient k_m reduces with an increase in the radiation parameter. Clearly, from Fig. 7B and C, we observed that both the entropy generation number and the Bejan number increases in the channel as the values thermal radiation parameter increases. This observation may be attributed to the dominance heat irreversibility. A similar observation is seen for the behavior of the temperature ratio parameter as illustrated in Fig. 8A to C.

Fig. 9 shows the effects of varying the Brinkman number within the range of $0 \leq Br \leq 7$ on the nanofluid profiles. We observed from Fig. 9A

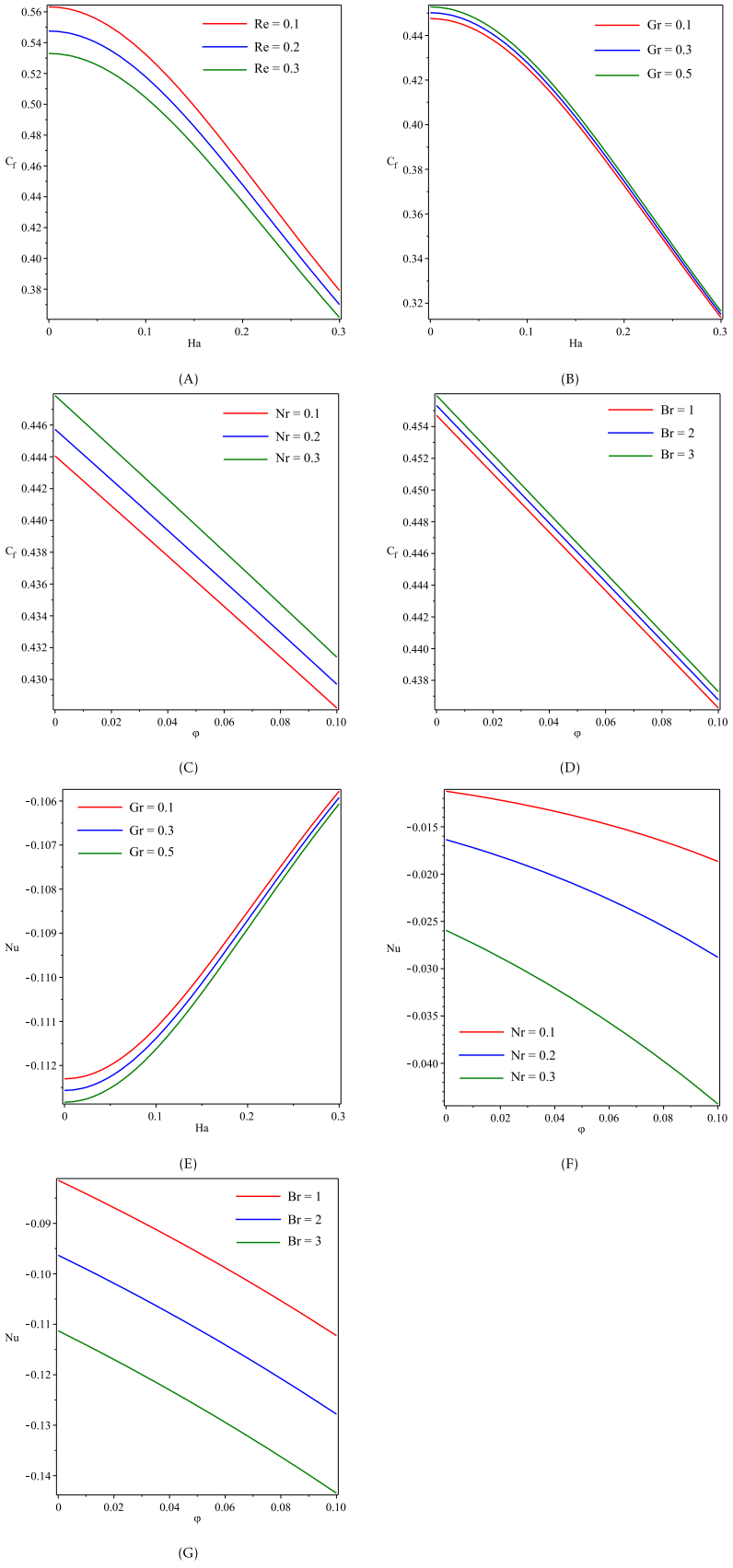

Fig. 11. (A) Effect of Reynolds number on skin friction coefficient, (B) effect of Grashof number on skin friction coefficient, (C) effect of radiation parameter on skin friction coefficient, (D) effect of Brinkman number on skin friction coefficient, (E) effect of Grashof number on Nusselt number, (F) effect of radiation parameter on Nusselt number, (G) effect of Brinkman number on Nusselt number.

that an increase in the values of the Brinkman number improves the temperature profiles. This is true, since increasing the magnitude of the Brinkman number implies an increase in the heat generated by dissipation which leads to a rise in the heat transfer rate within the channel. Fig. 9B shows the entropy generation number increases as the Brinkman number increases. Fig. 9C shows that in the absence of frictional heat irreversibility, the Bejan number is unity. Also, an increase in the Brinkman number decreases the Bejan number.

In Fig. 10, the effect of varying the Biot number on the nanofluid velocity profiles, temperature profiles, entropy generation number and Bejan number are illustrated. Fig. 10A to B shows that the nanofluid velocity profiles, as well as the temperature profiles, are enhanced with an increase in the Biot number. This is physically correct since increasing the values of the Biot number signifies an increase in the heat transfer coefficient, hence, the rate of cooling decreases while the temperature of the nanofluid within the channel rise. Both the entropy generation number and the Bejan number rises in the channel as seen in Fig. 10C to D.

The effects of various thermo-physical parameters on the skin friction and Nusselt number are illustrated in Fig. 11. We observed from these Figures that the skin friction decreases with increasing the values of Hartmann number, suction/injection Reynolds number and nanoparticle fraction volume but increases with an increase in Grashof number, thermal radiation parameter and Brinkman number. This can be attributed to a decrease or increase in nanofluid velocity gradient at the channel walls as the values of these parameters increases. Meanwhile, an increase in the Grashof number, thermal radiation parameter and Brinkman number decreases the Nusselt number due to a decrease in temperature gradient at the walls while an increase in Hartmann number and nanoparticle fraction volume increases the Nusselt number due to an increase in temperature gradient at the walls.

5. Conclusion

In this study, the entropy generation in a Powell-Eyring Al_2O_3-water nanofluid flow in a vertical channel subjected to convective cooling has been studied. The transport equations were solved using an iterative spectral local linearization method. The entropy generation rate in the system has been analyzed using the second law of thermodynamics. In summary, the nanoparticle volume fraction and the Brinkman number are significant in minimizing the entropy generation rate in the channel. Hence, by increasing the nanoparticle volume fraction and reducing the Brinkman number the flow in channel can be optimized.

Declarations

Author contribution statement

Hammed Abiodun Ogunseye: Analyzed and interpreted the data; Wrote the paper.

Precious Sibanda: Conceived and designed the analysis.

Funding statement

This research did not receive any specific grant from funding agencies in the public, commercial, or not-for-profit sectors.

Competing interest statement

The authors declare no conflict of interest.

Additional information

No additional information is available for this paper.

References

[1] S.U.S. Choi, Enhancing thermal conductivity of fluid with nanoparticles, developments and applications of non-Newtonian flow, in: ASME FED, vol. 231, 1995, pp. 95–105.
[2] K.V. Wong, O. De Leon, Applications of nanofluids: current and future, Adv. Mech. Eng. 2 (2010) 519–659.
[3] M. Sheikholeslami, M. Hatami, D.D. Ganji, Analytical investigation of MHD nanofluid flow in a semi-porous channel, Powder Technol. 246 (2013) 327–336.
[4] J. Raza, A.M. Rohni, Z. Omar, MHD flow and heat transfer of Cu–water nanofluid in a semi porous channel with stretching walls, Int. J. Heat Mass Transf. 103 (2016) 336–340.
[5] T. Hayat, M. Rashid, M. Imtiaz, A. Alsaedi, Magnetohydrodynamic (MHD) flow of Cu-water nanofluid due to a rotating disk with partial slip, AIP Adv. (2015).
[6] A. Malvandi, D.D. Ganji, Brownian motion and thermophoresis effects on slip flow of alumina/water nanofluid inside a circular microchannel in the presence of a magnetic field, Int. J. Therm. Sci. 84 (2014) 196–206.
[7] K. Das, P.R. Duari, P.K. Kumar, Solar radiation effects on Cu-water nanofluid flow over a stretching sheet with surface slip and temperature jump, Arab. J. Sci. Eng. 39 (2014) 9015–9023.
[8] R.E. Powell, H. Eyring, Mechanisms for the relaxation theory of viscosity, Nature 154 (1) (1994) 427–428.
[9] A. Tanveer, T. Hayat, F. Alsaadi, A. Alsaedi, Mixed convection peristaltic flow of Eyring-Powell nanofluid in a curved channel with compliant walls, Comput. Biol. Med. 82 (2017) 71–79.
[10] W.A. Khan, I. Pop, Boundary-layer flow of a nanofluid past a stretching sheet, Int. J. Heat Mass Transf. 53 (11) (2010) 2477–2483.
[11] T.M. Agbaje, S. Mondal, S.S. Motsa, P. Sibanda, A numerical study of unsteady non-Newtonian Powell-Eyring nanofluid flow over a shrinking sheet with heat generation and thermal radiation, Alex. Eng. J. 56 (1) (2017) 81–91.
[12] S. Hina, MHD peristaltic transport of Eyring-Powell fluid with heat/mass transfer, wall properties and slip conditions, J. Magn. Magn. Mater. 404 (2016) 148–158.
[13] T. Hayat, M.I. Khan, M. Waqas, A. Alsaedi, Effectiveness of magnetic nanoparticles in radiative flow of Eyring-Powell fluid, J. Mol. Liq. 231 (2017) 126–133.
[14] A. Bejan, Entropy Generation Minimization, CRC, Boca Raton, 1996.
[15] M. Pakdemirli, B.S. Yilbas, Entropy generation in a pipe due to non-Newtonian fluid flow: constant viscosity case, Sādhanā 31 (2006) 21–29.
[16] S. Das, A.S. Banu, R.N. Jana, O.D. Makinde, Entropy analysis on MHD pseudo-plastic nanofluid flow through a vertical porous channel with convective heating, Alex. Eng. J. 54 (3) (2015) 325–337.
[17] T.W. Ting, Y.M. Hung, N. Guo, Entropy generation of viscous dissipative nanofluid flow in thermal non-equilibrium porous media embedded in microchannels, Int. J. Heat Mass Transf. 81 (2015) 862–877.
[18] G. Ibáñez, Entropy generation in MHD porous channel with hydrodynamic slip and convective boundary conditions, Int. J. Heat Mass Transf. 80 (2015) 274–280.
[19] A. López, G. Ibáñez, J. Pantoja, J. Moreira, O. Lastres, Entropy generation analysis of MHD nanofluid flow in a porous vertical microchannel with nonlinear thermal radiation, slip flow and convective-radiative boundary conditions, Int. J. Heat Mass Transf. 107 (2017) 982–994.
[20] O.D. Makinde, A.S. Eegunjobi, Effects of convective heating on entropy generation rate in a channel with permeable walls, Entropy 15 (2013) 220–233.
[21] G. Nagaraju, S. Jangili, J.V. RamanaMurthy, O.A. Beg, A. Kadir, Second law analysis of flow in a circular pipe with uniform suction and magnetic field effects, J. Heat Transf. 141 (1) (2018) 012004.
[22] M. Sheikholeslam, New computational approach for exergy and entropy analysis of nanofluid under the impact of Lorentz force through a porous media, Comput. Methods Appl. Mech. Eng. 344 (2019) 319–333.
[23] S. Jangili, S.O. Adesanya, H.A. Ogunseye, R. Lebelo, Couple stress fluid flow with variable properties: a second law analysis, Math. Methods Appl. Sci. 42 (1) (2019) 85–98.
[24] M.I. Afridi, M. Qasim, Entropy generation and heat transfer in boundary layer flow over a thin needle moving in a parallel stream in the presence of nonlinear Rosseland radiation, Int. J. Therm. Sci. 123 (2018) 117–128.
[25] T. Hayat, F. Shaha, M.I. Khana, M. Imran Khan, A. Alsaedi, Entropy analysis for comparative study of effective Prandtl number and without effective Prandtl number via $\gamma Al_2O_3 - H_2O$ and $\gamma Al_2O_3 - C_2H_6O_2$ nanoparticles, J. Mol. Liq. 266 (2018) 814–823.
[26] S.O. Adesanya, H.A. Ogunseye, J.A. Falade, R.S. Lebelo, Thermodynamic analysis for buoyancy-induced couple stress nanofluid flow with constant heat flux, Entropy 19 (580) (2017).
[27] A.S. Eegunjobi, O.D. Makinde, MHD mixed convection slip flow of radiating Casson fluid with entropy generation in a channel filled with porous media, Defect Diffus. Forum 2017 (374) (2017) 47–66.
[28] M. Sheikholeslami, Omid Mahian, Enhancement of PCM solidification using inorganic nanoparticles and an external magnetic field with application in energy storage systems, J. Clean. Prod. 215 (2019) 963–977.
[29] C.T. Nguyen, F. Desgranges, N. Galanis, G. Roya, T. Maréd, S. Boucher, H. Angue Mintsa, Viscosity data for Al_2O_3–water nanofluid—hysteresis: is heat transfer enhancement using nanofluids reliable, Int. J. Therm. Sci. 47 (2008) 103–111.

[30] K. Khanafer, K. Vafai, A critical synthesis of thermophysical characteristics of nanofluids, Int. J. Heat Mass Transf. 54 (19) (2011) 4410–4428.
[31] S. Das, R.N. Jana, Natural convective magneto-nanofluid flow and radiative heat transfer past a moving vertical plate, Alex. Eng. J. 54 (1) (2015) 55–64.
[32] S.S. Motsa, A new spectral local linearization method for nonlinear boundary layer flow problems, J. Appl. Math. (2013) 423628, 15 pages.
[33] L.N. Trefethen, Spectral Methods in MATLAB, SIAM, 2000, p. 10.